ACS Catalysis

pubs.acs.org/acscatalysis

Research Article

Fabrication of Robust Covalent Organic Frameworks for Enhanced Visible-Light-Driven H_2 Evolution

Zhengfeng Zhao, Yunlong Zheng, Chun Wang, Sainan Zhang, Jie Song, Yafei Li, Shengqian Ma, Peng Cheng, Zhenjie Zhang,* and Yao Chen*

Cite This: *ACS Catal.* 2021, 11, 2098–2107

Read Online

ACCESS | Metrics & More | Article Recommendations | Supporting Information

ABSTRACT: Developing photocatalysts capable of visible-light-driven water splitting to produce clean hydrogen (H_2) is one of the premier challenges for solar energy conversion into clean and sustainable fuels. Inspired from the structure feature of photosystem I in nature, we have designed and synthesized a series of robust covalent organic frameworks (NKCOFs = Nankai University COFs) based on electric donor–acceptor moieties, in which the electron-donor group of pyrene can be used for harvesting light. Meanwhile, benzothiadiazole with different functional groups was introduced as an electron acceptor to tune the light-adsorption ability of COFs. Notably, the activity of NKCOF-108 for photochemical H_2 evolution under visible light was among the highest in COFs without hybridization with other materials. We attribute the high hydrogen evolution rate of NKCOF-108 to its distinct structural features and wide visible-light-response range. The highly ordered layered structure ensures that sufficient active sites are accessible for H_2 production, and the donor–acceptor design can promote the separation of photogenerated carriers. Our findings have provided an effective strategy to design photocatalysts for light-driven H_2 evolution.

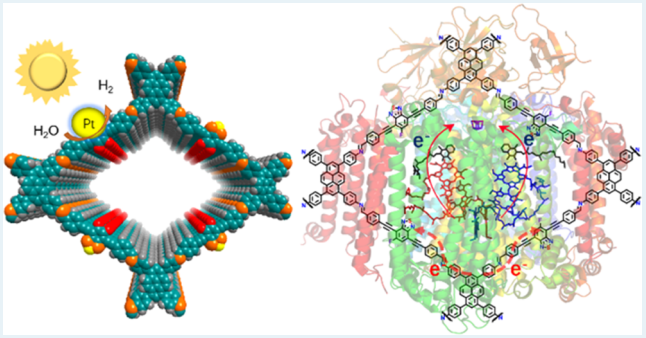

KEYWORDS: *covalent organic framework, photosystem I, photocatalysis, water splitting, H_2 evolution*

With the growing global demand for renewable and sustainable energy sources, light-driven water splitting to produce H_2 has become the ultimate goal for the supply of clean and sustainable energy.[1−5] Photosystem I (PS I) is well known to be the most efficient light converter in nature, which possesses quantum efficiency approaching 100%.[6] In PS I, the electron donors (P700, a dimer of chlorophyll *a*) and acceptors (iron–sulfur cluster) are arranged in ordered electron transfer (ET) cofactors (Scheme 1a).[7] This distinct donor–acceptor arrangement contributes to the high efficiency of PS I.[8] However, the vulnerable nature and the structural complexity of PS I hinder it from practical applications. Thus, developing highly efficient and robust artificial photosynthesis systems is of significant importance.

In the past few decades, increasing efforts have been made to fabricate organic conjugated polymers with electron-donor and -acceptor moieties for the conversion of solar energy into electric or chemical energy, owing to their advantages of high stability, excellent electrical/electrochemical activity, high carrier mobility, and mechanical properties.[9,10] However, traditional polymers usually displayed poor performance due to the relatively low charge transportability resulting from their lowly ordered structures,[11,12] narrow light-response range,[13] and strong recombination of photogenerated electron–hole

Scheme 1. (a) Symmetrical Features of ET Cofactors in PS I[a]

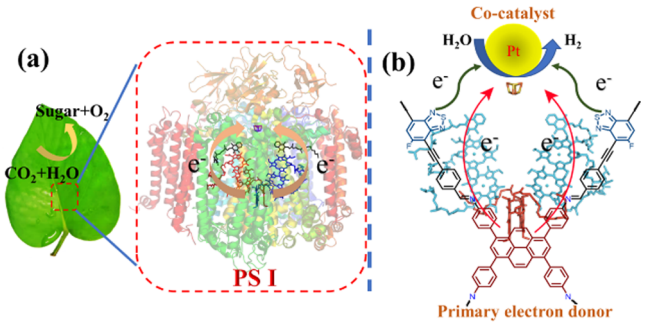

[a]The structure was derived from the 2.5 Å X-ray crystal structure of PS I from *Thermosynechococcus elongatus* (PDB file accession no. 1JB0). (b) The relationship of donor–acceptor moieties in PS I. P700 at the bottom of the symmetric geometry as the primary electron donor.[67] The iron–sulfur cluster acts as the electron acceptor.[68]

Received: November 5, 2020
Revised: January 21, 2021
Published: February 2, 2021

https://dx.doi.org/10.1021/acscatal.0c04820
ACS Catal. 2021, 11, 2098–2107

pairs.[14] Since 2005, covalent organic frameworks (COFs) have emerged as a new class of porous organic polymers with high crystallinity, designable structure, high porosity, tunable pore size, and customizable functionality for many potential applications.[15−28] Attributed to these features, COFs have shown great promise in overcoming the aforementioned drawbacks of traditional organic polymers.[9,12,29,30] Moreover, the highly ordered arrangement of functional moieties in COFs can facilitate their electrical conductivity, charge-carrier mobilities, and optical properties.[31−39]

Although a lot of COFs have been employed for H_2 evolution lately (Tables S1 and S2), such as hydrazone-linked **TFPT-COF**,[40] azine-linked COFs (**N_x-COF**),[41] diacetylene-functionalized COFs (**TP-BDDA COF**),[42] sulfone-containing COFs (**FS-COF**),[43] sp^2 carbon-jointed-pyridinyl frameworks (**g-$C_{40}N_3$-COFs**),[44] donor−acceptor COF (**sp^2 Carbon-COF_{ERDN}**),[45] and crystalline covalent triazine frameworks (**CTF-HUST-A1**),[46] the reported COFs still faced some drawbacks. (i) At present, the solar-to-hydrogen (STH) conversion efficiencies for reported COF photocatalysts[44,47] are far lower than the ideal solar-to-hydrogen conversion efficiency value.[48] (ii) Most pure COF photocatalysts have relatively low photocatalytic efficiency.[14,49] The COF-based photocatalysts with the highest efficiency were mostly fabricated via hybridizing COFs with other materials such as MOFs,[14] dyes,[43] and MXene.[49] The complicated hybridization process increased the synthesis challenge of photocatalysts. (iii) Moreover, the mechanism for the high performance of COF photocatalysts is still underexplored. With respect to these challenges, in this study, we adopted a rational strategy to create a series of highly efficient COF photocatalysts (**NKCOF-108**, **−109**, **−110**, and **−111**; NKCOF = Nankai University COFs) with donor−acceptor moieties.[45,50−56] After systematical optimization, **NKCOF-108** achieved high photocatalysis activity for H_2 production. Moreover, both experimental and simulation data unveiled in depth the mechanism for high performance.

In PS I,[57] the proteins fix the positions of electron donors and acceptors (Scheme 1a) while forming a symmetrical geometry and an ET path. P700 acts as the primary electron donor, and iron−sulfur clusters act as the electron acceptor (Scheme 1b). Inspired by the electron donor−acceptor in PS I, we used pyrene moieties[58,59] as the electron donor and designed various electron acceptor moieties[50,60] for photocatalytic H_2 evolution. Meanwhile, we introduced alkynyl groups as a bridge between electron donors and accepters to achieve an efficient transfer of photogenerated electrons.[61,62] In this study, benzothiadiazole and its fluorinated derivatives (Figure 1a) were chosen as electron acceptors based on the following considerations. Attributed to the N atoms with higher electronegativity and C═N groups with lower-energy π-orbital, benzothiadiazole exhibits a strong electron-withdrawing property.[60,63,64] Moreover, the introduction of electronegative fluorine groups can efficiently enhance the performance of the electron acceptor.[65,66] In addition, to highlight the advantage of benzothiadiazole moieties, the phenylene group as the electron acceptor was introduced for comparison (Figure 1a).

A pyrene tetraamine (Figure 1a) was employed as a comonomer to react with dialdehydes, considering its conjugated structure and high symmetry that facilitate the formation of highly crystalline frameworks. Four isostructural COFs (**NKCOF-108**, **−109**, **−110**, and **−111**) with a two-dimensional (2D) layered packing structure and one-dimensional (1D) tetragonal channels (Figure 1b) were synthesized via a Schiff-base condensation reaction under solvothermal conditions (Figures 1a and S1−S4).[59] Powder X-ray diffraction (PXRD) analyses elucidated the high crystallinity of the as-synthesized COFs (Figure 2). Moreover, fully eclipsed AA layer stacking and staggered AB layer stacking models were constructed (Figure S5). Geometry optimizations of the structural models were conducted using the Materials Studio software package. The experimental PXRD patterns agreed well with the patterns simulated from an AA-eclipsed layer stacking model. **NKCOF-108**, **−109**, and **−110** possess a space group of P222 while **NKCOF-111** possesses a space group of *PBAN* due to the higher symmetry of the dialdehyde monomer with phenyl as the symmetry center. The PXRD patterns are dominated by an intense reflection in the low-angle region at 2.4° (2θ) for all COFs, which can be assigned to the primitive tetragonal lattice with an inplane lattice parameter of ∼35 Å. The Pawley-refined patterns of NKCOFs (blue curve) with low R_{wp} and R_p values (Figure 2) confirmed the correctness of peak assignments, as evidenced by negligible deviation from the observed PXRD patterns (red cycle). The unit cell parameters of the refinement AA stacking models and the coordinates of the simulated structures are provided in the Supporting Information (Figure S5 and Tables S3−S6). Notably, NKCOFs exhibited good chemical stability. After various treatments, such as boiling water, organic solvents, aqueous HCl (pH 1), and NaOH (1 M) solutions, all NKCOFs retained their original PXRD profiles (Figure S6a−d). Moreover, NKCOFs exhibited nearly no significant weight loss in boiling water and organic solvents (Figure S6e), indicative of their high solvent stability.

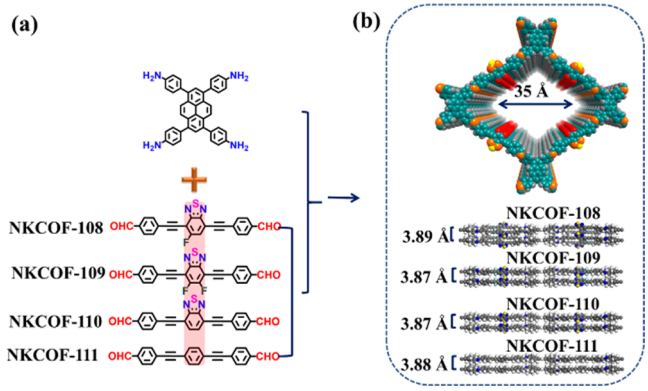

Figure 1. (a) Monomers of the NKCOFs. (b) Structural models for NKCOFs with perfectly eclipsed AA stacking shown parallel to the pore channel along the crystallographic *c* axis (top) and parallel to the tetragonal layers (bottom).

The Fourier transform infrared (FT-IR) spectra reveal a stretching vibration band at 1627 cm^{-1} assigned to the C═N bonds for NKCOFs (Figure 3a). The C═O and N−H signals at 1692 and 3360 cm^{-1} were observed corresponding to the terminal $-NH_2$ and −CHO group on the surface of all NKCOFs, respectively. Specifically, all NKCOFs showed a peak at 2190 cm^{-1} that was assigned to the stretching bands of C≡C triple bond. As shown in Figure 3b, the ^{13}C cross-polarization magic-angle spinning (CP-MAS) ssNMR spectrum of **NKCOF-108** exhibits a set of signals between 80 and 160 ppm that originates from the aromatic carbons in the framework. The carbon signals of C═N and C-F on the

https://dx.doi.org/10.1021/acscatal.0c04820
ACS Catal. 2021, 11, 2098−2107

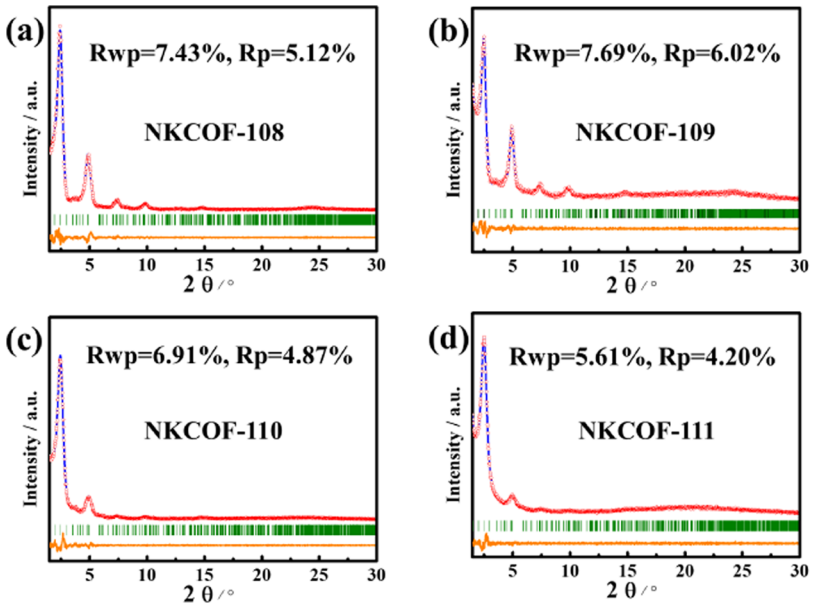

Figure 2. Experimentally observed PXRD patterns (red cycle), Pawley-refined patterns (blue line), the Bragg positions (green line), and the difference between experimental and calculated data (orange line) of (a) **NKCOF-108**, (b) **NKCOF-109**, (c) **NKCOF-110**, and (d) **NKCOF-111** for AA stacking.

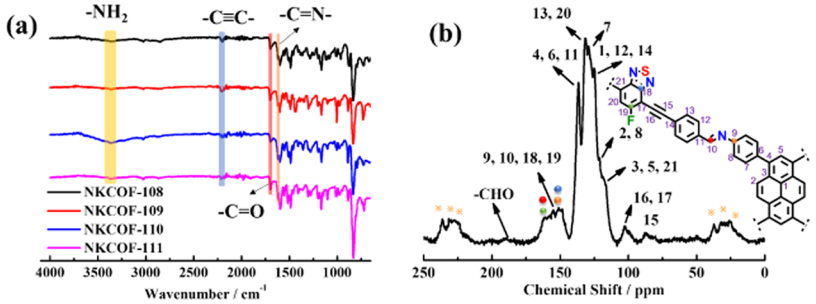

Figure 3. (a) FT-IR spectra of NKCOFs. (b) ^{13}C CP-MAS ssNMR spectrum of **NKCOF-108**. Spinning sidebands are marked with asterisks.

benzothiadiazole moiety and C═N of imine groups overlapped at 140−165 ppm. Additionally, the signals of C≡C and −CHO carbons were located at 105−85 and 189 ppm, respectively, and the peaks for other aromatic carbon atoms ranged from 110 to 140 ppm. A full assignment of all resonances for other ^{13}C CP-MAS ssNMR spectra of NKCOFs is shown in Figure S7.

Nitrogen sorption isotherms were collected at 77 K to examine the porosity of NKCOFs. As shown in Figures 4a and S8 and S9, the isotherms of all COFs exhibit the typical type-IV isotherm with a steep increase at low relative pressures, indicating the mesoporous nature. The Brunauer−Emmett−Teller (BET) specific surface areas were calculated to be 1880, 1540, 1230, and 1150 $m^2\ g^{-1}$, and the Langmuir specific surface areas were calculated to be 3056, 3239, 1802, and 1900 $m^2\ g^{-1}$ for **NKCOF-108**, **−109**, **−110**, and **−111**, respectively. The pore-size distribution calculated using the density functional theory (DFT) revealed uniform mesosized pores of ∼35 Å for NKCOFs (Figures 4a and S9), which are in excellent agreement with the mesoporous features from structural analysis and simulations. The high porosity and mesopores can ensure NKCOFs with sufficient active sites accessible for H_2 evolution and benefit the ingress of reactants (i.e., H_2O, ascorbic acid) and diffusion of products (i.e., H_2).

The morphological features of the as-synthesized COFs were characterized using scanning electron microscopy (SEM) (Figures 4b and S10). SEM images revealed that **NKCOF-108**, **−109**, and **−110** present particles with fibrous morphology, while **NKCOF-111** exhibited cottonlike aggregated particles. Furthermore, high-resolution transmission electron microscopy (HRTEM) was used to confirm the formation of a periodic framework for NKCOFs. Notably, HRTEM images reveal the distinct 1D channels (the side views of the pore) with a uniform diameter of ∼3 nm (Figures 4c and S11), which is consistent with the pore diameter (∼3 nm) of the simulated COF structure with AA stacking.[41,44] Additionally, all NKCOFs show similar lattice fringes (Figures 4d and S12), indicative of the ordered alignment with a high degree of crystallinity. The periodic patterns of ∼0.35 nm can be observed for all COFs, corresponding to the π-stacked 2D covalent sheets.

The UV/vis diffuse reflectance spectra show the strong absorption of NKCOFs in both the UV and visible regions (Figure 5a). Moreover, the light-absorption ability of NKCOFs can be fine-tuned by adjusting electron acceptors. **NKCOF-111** (phenylene as the acceptor) presents the narrowest light response among all NKCOFs. With benzothiadiazole derivatives as electron acceptors, **NKCOF-108**, **−109**, and **−110** show different degrees of red shift in the optical absorption

https://dx.doi.org/10.1021/acscatal.0c04820
ACS Catal. 2021, 11, 2098−2107

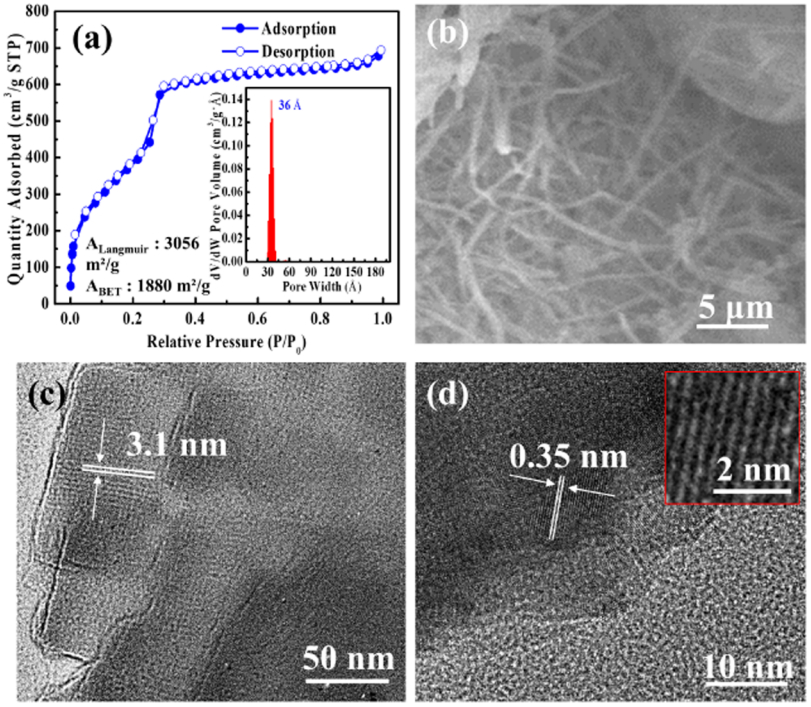

Figure 4. (a) N_2 adsorption (solid symbols) and desorption (open symbols) isotherms of **NKCOF-108** at 77 K. The inset shows the pore-size distribution of **NKCOF-108**. (b) Scanning electron microscopy (SEM) images of **NKCOF-108**. (c, d) High-resolution transmission electron microscopy (HRTEM) images of **NKCOF-108**. The inset shows the high-resolution image of the lattice fringes.

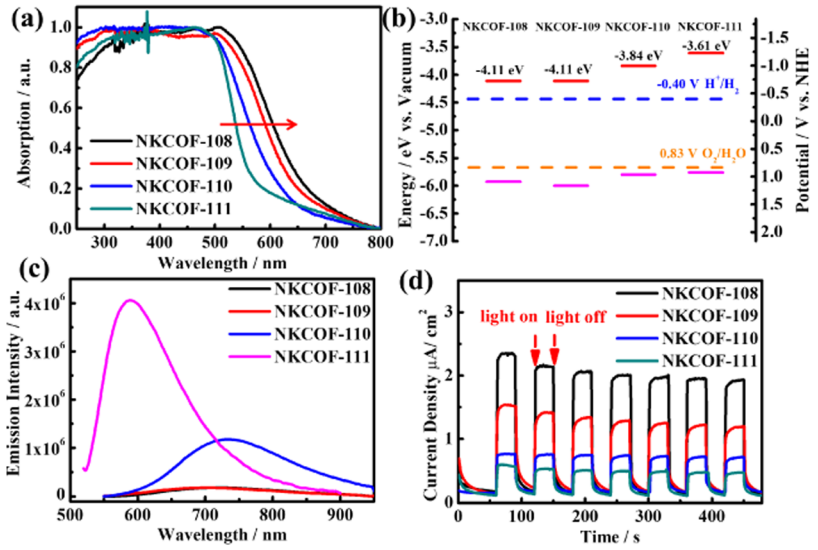

Figure 5. (a) UV/vis diffuse reflectance spectra of NKCOFs. (b) The band edge positions of NKCOFs (these vacuum-level values were converted to electrochemical potentials as follows: −4.44 eV vs vacuum level is equal to −0.0 V vs normal hydrogen electrode (NHE) at pH 7); HOMO = LUMO − E_g. (c) Steady-state photoluminescence (PL) spectra for the NKCOFs. Photoexcitation was achieved with a picosecond diode laser at 510 nm. (d) Photocurrent measurements for the NKCOFs in 0.1 M Na_2SO_4 solution (a Ag/AgCl reference electrode) under visible light (>420 nm) irradiation.

onset from 500 to 700 nm compared with **NKCOF-111**. It was found that the introduction of fluoride groups on benzothiadiazole units (**NKCOF-108** and **−109**) can significantly promote light absorption, and **NKCOF-108** with monofluorinated benzothiadiazole exhibits the widest light-absorption range. The optical band gaps (E_g) of **NKCOF-108**, **−109**, **−110**, and **−111** were determined to be 1.82, 1.89, 1.96, and 2.15 eV, respectively, according to the Kubelka−Munk function (Figure S13). To further understand the enhanced visible-light responses and investigate the highest occupied molecular orbital (HOMO) and the lowest unoccupied molecular orbital (LUMO) levels, cyclic voltammetry measurements of the NKCOFs were recorded (Figures S14 and S15). As shown in Figure 5b, LUMO levels of all COFs are well-positioned for visible-light-driven H_2 production from water splitting. To gain more insight into the trend of energy levels, Mott−Schottky analysis was conducted (Figure S16). It is clearly presented that all photoanodes exhibit positive slopes,

https://dx.doi.org/10.1021/acscatal.0c04820
ACS Catal. 2021, 11, 2098−2107

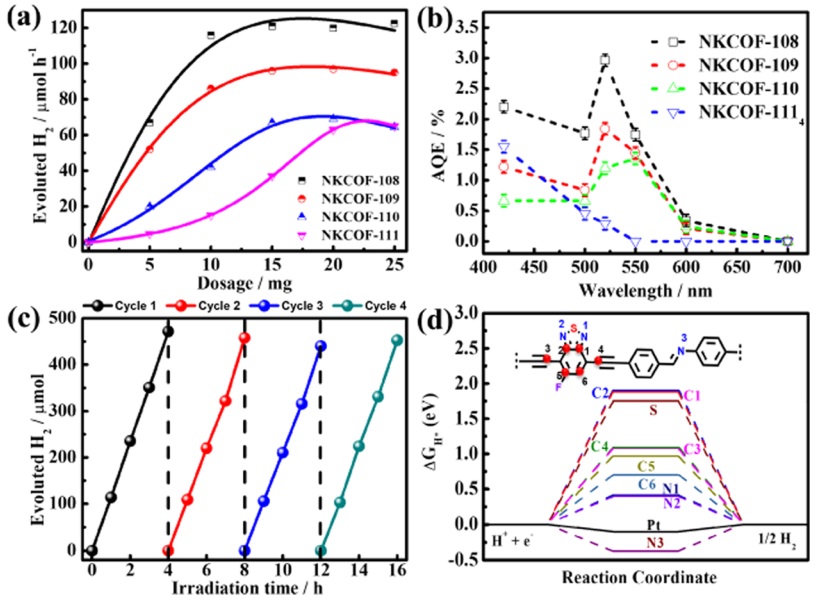

Figure 6. (a) Optimization of the photocatalyst quality for the maximum average hydrogen production rate in 4 h. (b) Apparent quantum efficiency (AQE) values of the photocatalysts under the conditions of maximum hydrogen production rate according to (a) (λ = 420 ± 10, 500 ± 10 520 ± 10, 550 ± 10, 600 ± 10, and 700 ± 10 nm; **NKCOF-108** and **109**: 15 mg, **NKCOF-110**: 20 mg, **NKCOF-111**: 25 mg). (c) Long-term H_2 evolution test of **NKCOF-108** monitored over 16 h with evacuation every 4 h. (d) Hydrogen-binding free energy, ΔG_{H^*}, at nitrogen, sulfur, and carbon sites in the case of one hydrogen atom.

showing n-type semiconductor features. The flat-band potentials (E_{fb}) display a gradually negative shift from the **NKCOF-108** to **−111** photoanode. The E_{fb} of **NKCOF-108**, **−109**, **−110**, and **−111** are fitted to be −0.31, −0.31, −0.40, and −0.51 V vs normal hydrogen electrode (NHE), respectively. In addition, the E_{fb} of all COFs is more positive than their LUMO levels, which is a common phenomenon in an n-type semiconductor.[69] These results suggested that the boosted visible light responses resulted from the downshifted LUMO and HOMO energy levels of NKCOFs, attributed to the contribution of the fluorine atom.[66] Furthermore, the similar trends of HOMO and LUMO levels were also confirmed by density functional theory (DFT) calculations (Figure S17a). The density of states (DOS) of NKCOFs (Figure S17b) revealed that HOMO and LUMO levels were mainly contributed by the 2p orbital of C atoms, demonstrating that the photogenerated electrons are from π-delocalization. Therefore, modification of electron acceptors with different functional groups provides an effective strategy to optimize the photoredox potentials of COFs.

Further insight into the electron transfer behavior was revealed by steady-state photoluminescence (PL) spectra and photocurrent experiments (Figure 5c,d). As compared with **NKCOF-111**, the red-shifted main peaks of **NKCOF-108**, **−109**, and **−110** can be observed corresponding to their wider visible-light-response range (Figures 5a and S18). Besides, the downward trend of PL intensity (**NKCOF-108** ≈ **NKCOF-109** < **NKCOF-110** < **NKCOF-111**) indicated that the recombination of photoexcited electron−hole pairs was significantly suppressed.[70,71] This was further verified by their time-resolved fluorescence emission decay spectra (Figure S19) and enhanced photocurrent intensity (Figure 5d). NKCOFs showed triexponential decay curves. **NKCOF-111** presented the shortest fluorescence lifetime, which reflected its high carrier recombination rate. The shorten fluorescence lifetime from **NKCOF-110** to **−108** may be caused by the charge transfer in the framework.[72] In addition, the HOMO electrons are distributed mainly on electron-rich aromatic carbon skeletons, whereas the LUMO electrons are mainly focused on electron-deficient benzothiadiazole and its fluorinated derivatives units (Figure S20). The DFT calculation results further suggested that benzothiadiazole and its derivatives units were more favorable for π-delocalization. The photocurrent intensity with a reproducible response generated by NKCOFs indicates that the photo-induced carriers transferred on the photoelectrode. NKCOFs with different electron acceptors showed an obviously different long-term steady photocurrent density response. The trend of the generated photocurrent density for NKCOFs is consistent with that of the photocatalytic hydrogen evolution rate (HER). These results indicated that benzothiadiazole derivatives facilitate efficient charge-carrier transport and electron delocalization in COFs. **NKCOF-108** showed the highest photocurrent density among all NKCOFs, indicating that the monofluorinated benzothiadiazole unit is more conducive in separating the photogenerated charges.

H_2 evolution experiments were performed by irradiating a suspension of photocatalysts in a 100 mL aqueous solution (Figure S21) using ascorbic acid as a sacrificial electron donor and Pt as a cocatalyst with visible light (λ > 420 nm) at 5 °C (Labsolar−IIIAG, Beijing Perfectlight). Interestingly, pure NKCOFs (10 mg) without the Pt cocatalyst can enable steady production of H_2 with an average hydrogen evolution rate (HER) of 0.50, 0.42, 0.40, and 0.35 μmol h^{-1} for **NKCOF-108**, **−109**, **−110**, and **−111** (Figure S22), respectively. To explore if the residual Pd is attributed to the H_2 production, the contents of residual Pd in NKCOFs were determined by inductively coupled plasma mass spectrometry (ICP-MS). Less than 0.05 wt % of Pd was found for all NKCOFs. Furthermore, X-ray photoelectron spectroscopy (XPS) (Figure S23) and energy-dispersive X-ray (EDX) spectroscopy (Figure S24) did not detect signals for Pd due to its extremely low content. To

https://dx.doi.org/10.1021/acscatal.0c04820
ACS Catal. 2021, 11, 2098−2107

further improve the hydrogen evolution performance, Pt, a widely used cocatalyst,[73] was in situ deposited into the network of NKCOFs according to the common literature method. We systematically investigated the correlation between the H_2 production rate and the Pt loading amount. After optimization, 5 wt % Pt-modified **NKCOF-108** achieved the best performance (Figure S25).

To make full use of light sources, we attempted to optimize the photocatalyst quality for the maximum hydrogen evolution rate (Figures 6a and S26). We found the trend of the HER to be **NKCOF-108** > **NKCOF-109** > **NKCOF-110** > **NKCOF-111**. The HER of **NKCOF-108** reached up to 120 μmol h^{-1} under optimized conditions. This result suggests that benzothiadiazole and fluorine groups are crucial for high photocatalytic performance. Under the optimized conditions, the enhanced visible-light HER of **NKCOF-108** with the Pt cocatalyst can also be attributed to the wide light-absorption range, as expressed in the apparent quantum efficiency (AQE) at 420, 500, 520, 550, 600, and 700 nm when using monochromatic light (Figure 6b and Table S7). The AQE decreased with increasing wavelength, and the longest wavelength capable of triggering the reaction coincided with the optical absorption onset of NKCOFs. These results clearly prove that the light conversion efficiency is highly dependent on the light-response range of NKCOFs (Figure S13b). Besides, **NKCOF-108** showed higher AQE values at each wavelength (2.96% at 520 nm) than those of other NKCOFs. These results indicated that monofluorinated benzothiadiazole promoted effective utilization of light.

Notably, **NKCOF-108** showed a remarkably high HER (120 μmol h^{-1}) (Figure S27). Besides, HERs with surface area normalized were also estimated (Figure S27c), which exhibited a similar trend as the above result. Two widely studied photocatalysts **P25** (TiO_2) and polymeric carbon nitride (**PCN**) were selected for comparison under the same experimental conditions. **PCN** was synthesized by calcination of urea at 550 °C,[73] and the related characterizations are shown in Figure S28. Negligible H_2 was detected for **P25** because it barely absorbed visible light. The **PCN** showed a low HER of 5.5 μmol h^{-1}, which was 21 times lower than that of **NKCOF-108**. To highlight the advantage of crystalline polymers compared with amorphous polymers, an amorphous phase of **NKCOF-108** was synthesized with the same monomers (the PXRD pattern shown in Figure S29a). During the photocatalysis test, amorphous **NKCOF-108** showed a stable HER of 76 μmol h^{-1}, which is 1.5 times lower than that of crystalline **NKCOF-108** (Figure S29b). The surface-area-normalized HERs for **NKCOF-108** and its amorphous phase were also calculated and compared (Figure S29). Compared with **NKCOF-108**, the reduced photocurrent density of amorphous **NKCOF-108** suggested the suppressed recombination of photocarriers by the crystalline structure (Figure S30). These results clearly demonstrated that materials' crystallinity has a positive effect on their photocatalysis performance.

Moreover, the photostability of **NKCOF-108** was confirmed via testing long-term H_2 evolution (Figure 6c). The steady HER without significant decay can be observed during the photocatalysis experiment (16 h) for **NKCOF-108** under visible light irradiation (λ > 420 nm). After the photoreaction, PXRD data revealed that **NKCOF-108** retained its crystallinity (Figure S31). Furthermore, FT-IR spectra (Figures S32) of all NKCOFs recycled after photocatalysis did not show any significant changes. These results suggest the outstanding stability and reusability of **NKCOF-108**.

According to previous research, benzothiadiazole is the main active site for hydrogen production. Therefore, DFT calculations were carried out to investigate the H_2 evolution reaction pathways on possible active sites around monofluorinated benzothiadiazole. As shown in Figure 6d, there is a distinct difference in hydrogen-binding free energy (ΔG_{H^*}) when different sites are hydrogenated. The high hydrogen-binding free energy at the sulfur and carbon sites proved that there is a high overpotential for the HER, whereas the hydrogen-binding free energy ΔG_{H^*} at the nitrogen sites decreased to about 0.42, 0.40, and −0.37 eV for N1, N2, and N3, respectively, showing that the addition of benzothiadiazole units and imine linkage in **NKCOF-108** leads to stronger hydrogen adsorption, which in turn favors the energetics toward H_2 formation.

During the photocatalytic H_2 evolution experiments, Pt nanoparticles were photodeposited on the surface of the samples. In other words, the deposition site of Pt corresponds to the terminal point of the photogenerated electron transfer in the framework. XPS tests have been used to analyze the position of Pt loaded on NKCOFs. High-resolution Pt 4f XPS spectra of all NKCOFs after photocatalysis could be deconvoluted into two pairs of peaks corresponding to Pt^0 and Pt^{2+} on the basis of database values (Figure S33). Pt^0 was effective for H_2 evolution, while Pt^{2+} was from the oxide on the surface of Pt^0 and coordination with NKCOFs. By comparing the samples before and after photocatalytic H_2 production, we found that the binding energy of benzothiadiazolyl N 1s, F 1s, and S 2p orbitals were changed. Besides, the high binding-energy shift of terminal $-NH_2$ N 1s can also be observed. Simultaneously, the binding energy of imine N 1s orbitals did not show any change in **NKCOF-108**, **−109**, and **−110** (Figures S34−S37). These XPS results indicated the strong interaction among Pt, benzothiadiazole, and its fluorinated derivative units. Therefore, benzothiadiazolyl N and S can anchor the Pt cation, and these sites can donate electrons to reduce the Pt cation to form Pt nanoparticles for H_2 production during illumination.

To explore the true active sites on different NKCOFs, we performed an in situ FT-IR test for the NKCOFs.[74] The peak of C═N on benzothiadiazole overlapped with that of C═O, which was absent before illumination. Under light irradiation, the peak at 1670 cm^{-1} that was assigned to the C═N on benzothiadiazole gradually appeared on the FT-IR spectra of **NKCOF-108**, **−109**, and **−110** (Figure S38) because of the accumulation of charges. By contrast, the FT-IR spectra of **NKCOF-111** without benzothiadiazole groups showed no significant changes before and after illumination. After adsorbing ascorbic acid, this peak did not appear in the FT-IR spectra for all NKCOFs under light irradiation (Figure S39). These results revealed that the true active sites on **NKCOF-108**, **109**, and **110** could be the N sites on benzothiadiazole. According to the XPS results (Figure S34d) and the literature,[75] the active sites of **NKCOF-111** may be the N sites on the imine bond that bridged monomers. These inferences were consistent with the DFT calculation results.

The major differences between NKCOFs lie in their different acceptor units, leading to the difference in optical properties. The broad light-harvesting range and improved separation of photogenerated electron−hole pairs by introduc-

https://dx.doi.org/10.1021/acscatal.0c04820
ACS Catal. 2021, 11, 2098−2107

ing acceptor units (**NKCOF-108**, **−109**, and **−110**) are the important factors to improve the photocatalytic activity. In addition, the photogenerated electron transfer behavior also plays a crucial role in the enhanced photocatalytic performance. It should be noted that photocatalytic H_2 production can be achieved only when the photogenerated electrons are transferred to the active sites. Therefore, it is necessary to ensure that more photogenerated electrons can be transferred to the H_2 production active sites when using strong acceptor units.

The photoelectron transfer pathway in these NKCOFs can be inferred and are displayed in Figure S40. It is well established that the charges tend to transfer to the acceptor units in the donor−acceptor polymers.[76,77] Due to the introduction of benzothiadiazole and its derivatives as acceptor units, **NKCOF-108**, **−109**, and **−110** showed higher photocatalytic activity than **NKCOF-111**. However, the limited electron-withdrawing ability of benzothiadiazole leads to the decrease of the light-absorption ability of **NKCOF-110**, and the active sites (nitrogen sites on benzothiadiazole) in **NKCOF-110** cannot efficiently concentrate the photogenerated electrons for H_2 production. To obtain stronger acceptor units, F atoms were introduced into benzothiadiazole. **NKCOF-108** and **−109** with stronger electron acceptors (i.e., fluorinated benzothiadiazole) than **NKCOF-110** exhibited enhanced photocatalytic performance compared to **NKCOF-110**. **NKCOF-109** with the difluorinated benzothiadiazole unit showed lower photocatalytic performance than **NKCOF-108** with the monofluorinated benzothiadiazole unit. This should result from the transfer paths of photogenerated electrons in these NKCOFs. The photogenerated electrons cannot be delivered to N sites for H_2 production in **NKCOF-108** and **−109** with strongly electrophilic F atoms.[78] F atoms can extract the photogenerated electrons in NKCOFs, and the high content of F atoms in **NKCOF-109** leads to the decreased number of electrons for photocatalytic reaction. Therefore, a balance between the strength of acceptor units and the content of F atoms on benzothiadiazole should be taken into full consideration to realize an optimized performance in photocatalytic H_2 production. Monofluorinated benzothiadiazoles in **NKCOF-108** can not only ensure the strength of the acceptor unit but also make the photogenerated electrons transfer to the active sites as much as possible. As a result, **NKCOF-108** showed the highest photocatalytic performance among all NKCOFs. In the presence of Pt, the N sites (active sites) can anchor Pt and tend to donate electrons to Pt nanoparticles for H_2 production. Therefore, the Pt-modified NKCOFs showed higher photocatalytic performance than the pure COF systems.

In conclusion, we have created a rational design strategy to employ benzothiadiazole and its derivatives as electron acceptors to construct a series of 2D COFs (NKCOFs) with high crystallinity, high porosity, and good stability. We found that the modification of electron acceptors with different functional groups (e.g., fluorine) can efficiently adjust the photoredox potentials and broaden the light-response range of NKCOFs via adjusting their HOMO and LUMO levels. The excellent light-harvesting characteristics and appropriate band energy levels of NKCOFs render them perfect candidates as photocatalysts for H_2 evolution from water. After optimization, **NKCOF-108** exhibited enhanced photocatalytic performances (HER = 120 μmol h^{-1}) with the AQE as 2.96% at 520 nm among NKCOFs. We attributed the outstanding performance of **NKCOF-108** to the following factors: (i) its wide light-response range promotes efficient harvesting of low-energy photons for photocatalytic H_2 production, (ii) its high crystallinity and surface area ensure sufficient active sites accessible for H_2 production, and (iii) the highly ordered layered structure promotes mobility and separation of photogenerated carriers. This study not only provides valuable guidance for the rational design of COFs as highly efficient photocatalysts but also opens up an effective avenue to construct robust and reusable photocatalysts.

■ ASSOCIATED CONTENT

Supporting Information

The Supporting Information is available free of charge at https://pubs.acs.org/doi/10.1021/acscatal.0c04820.

Materials and methods; synthesis procedures; supplementary structural figures; and supplementary characterization data and crystal data (CIF); hydrogen generation activities of pure COFs photocatalysts without hybridization of other materials; hydrogen generation activities for all COFs anticipated photocatalysts; fractional atomic coordinates of the **NKCOF-108** unit cell (PDF)

■ AUTHOR INFORMATION

Corresponding Authors

Zhenjie Zhang − *State Key Laboratory of Medicinal Chemical Biology, College of Pharmacy, College of Chemistry, and Key Laboratory of Advanced Energy Materials Chemistry, Ministry of Education, Nankai University, Tianjin 300071, China;* orcid.org/0000-0003-2053-3771; Email: zhangzhenjie@nankai.edu.cn

Yao Chen − *State Key Laboratory of Medicinal Chemical Biology, College of Pharmacy, Nankai University, Tianjin 300071, China;* orcid.org/0000-0002-3465-7380; Email: chenyao@nankai.edu.cn

Authors

Zhengfeng Zhao − *State Key Laboratory of Medicinal Chemical Biology, College of Pharmacy, Nankai University, Tianjin 300071, China*

Yunlong Zheng − *State Key Laboratory of Medicinal Chemical Biology, College of Pharmacy, Nankai University, Tianjin 300071, China*

Chun Wang − *Jiangsu Collaborative Innovation Centre of Biomedical Functional Materials, Jiangsu Key Laboratory of New Power Batteries, School of Chemistry and Materials Science, Nanjing Normal University, Nanjing, Jiangsu 210023, China*

Sainan Zhang − *State Key Laboratory of Medicinal Chemical Biology, College of Pharmacy, Nankai University, Tianjin 300071, China*

Jie Song − *State Key Laboratory of Medicinal Chemical Biology, College of Pharmacy, Nankai University, Tianjin 300071, China*

Yafei Li − *Jiangsu Collaborative Innovation Centre of Biomedical Functional Materials, Jiangsu Key Laboratory of New Power Batteries, School of Chemistry and Materials Science, Nanjing Normal University, Nanjing, Jiangsu 210023, China;* orcid.org/0000-0003-2587-820X

Shengqian Ma − *Department of Chemistry, University of North Texas, Denton, Texas 76201, United States;* orcid.org/0000-0002-1897-7069

https://dx.doi.org/10.1021/acscatal.0c04820
ACS Catal. 2021, 11, 2098−2107

Peng Cheng − *College of Chemistry and Key Laboratory of Advanced Energy Materials Chemistry, Ministry of Education, Nankai University, Tianjin 300071, China;* orcid.org/0000-0003-0396-1846

Complete contact information is available at: https://pubs.acs.org/10.1021/acscatal.0c04820

Notes

The authors declare no competing financial interest.

■ ACKNOWLEDGMENTS

The authors acknowledge the financial support from the National Key Research and Development Program of China (2020YFA0907300), the National Natural Science Foundation of China (21871153, 31800793), and 111 Project (B12015). We also thank Professor Hangxun Xu's team from the University of Science and Technology of China and Shengli Zhu's team from Tianjin University for their assistance in evaluating the photocatalytic performance.

■ REFERENCES

(1) Hisatomi, T.; Kubota, J.; Domen, K. Recent Advances in Semiconductors for Photocatalytic and Photoelectrochemical Water Splitting. *Chem. Soc. Rev.* **2014**, *43*, 7520−7535.
(2) Tong, H.; Ouyang, S.; Bi, Y.; Umezawa, N.; Oshikiri, M.; Ye, J. Nano-photocatalytic Materials: Possibilities and Challenges. *Adv. Mater.* **2012**, *24*, 229−251.
(3) Wang, H.; Zhang, L.; Chen, Z.; Hu, J.; Li, S.; Wang, Z.; Liu, J.; Wang, X. Semiconductor Heterojunction Photocatalysts: Design, Construction, and Photocatalytic Performances. *Chem. Soc. Rev.* **2014**, *43*, 5234−5244.
(4) Dai, C.; Liu, B. Conjugated Polymers for Visible-light-driven Photocatalysis. *Energy Environ. Sci.* **2020**, *13*, 24−52.
(5) Su, T.; Shao, Q.; Qin, Z.; Guo, Z.; Wu, Z. Role of Interfaces in Two-Dimensional Photocatalyst for Water Splitting. *ACS Catal.* **2018**, *8*, 2253−2276.
(6) Croce, R.; van Amerongen, H. Light-Harvesting in Photosystem I. *Photosynth. Res.* **2013**, *116*, 153−166.
(7) Milanovsky, G.; Gopta, O.; Petrova, A.; Mamedov, M.; Gorka, M.; Cherepanov, D.; Golbeck, J. H.; Semenov, A. Multiple Pathways of Charge Recombination Revealed by the Temperature Dependence of Electron Transfer Kinetics in Cyanobacterial Photosystem I. *Biochim. Biophys. Acta, Bioenerg.* **2019**, *1860*, 601−610.
(8) Fetisova, Z. G.; Freiberg, A. M.; Timpmann, K. E. Long-range Molecular Order as An Efficient Strategy for Light Harvesting in Photosynthesis. *Nature* **1988**, *334*, 633−634.
(9) Long, Y.-Z.; Li, M.-M.; Gu, C.; Wan, M.; Duvail, J.-L.; Liu, Z.; Fan, Z. Recent Advances in Synthesis, Physical Properties and Applications of Conducting Polymer Nanotubes and Nanofibers. *Prog. Polym. Sci.* **2011**, *36*, 1415−1442.
(10) Sun, Q.; Dai, Z.; Meng, X.; Wang, L.; Xiao, F.-S. Task-Specific Design of Porous Polymer Heterogeneous Catalysts beyond Homogeneous Counterparts. *ACS Catal.* **2015**, *5*, 4556−4567.
(11) Vohra, V.; Kawashima, K.; Kakara, T.; Koganezawa, T.; Osaka, I.; Takimiya, K.; Murata, H. Efficient Inverted Polymer Solar Cells Employing Favourable Molecular Orientation. *Nat. Photonics* **2015**, *9*, 403−408.
(12) Liu, Y.; Zhao, J.; Li, Z.; Mu, C.; Ma, W.; Hu, H.; Jiang, K.; Lin, H.; Ade, H.; Yan, H. Aggregation and Morphology Control Enables Multiple Cases of High-efficiency Polymer Solar Cells. *Nat. Commun.* **2014**, *5*, No. 5293.
(13) Lin, L.; Yu, Z.; Wang, X. Crystalline Carbon Nitride Semiconductors for Photocatalytic Water Splitting. *Angew. Chem., Int. Ed.* **2019**, *58*, 6164−6175.
(14) Zhang, F. M.; Sheng, J. L.; Yang, Z. D.; Sun, X. J.; Tang, H. L.; Lu, M.; Dong, H.; Shen, F. C.; Liu, J.; Lan, Y. Q. Rational Design of MOF/COF Hybrid Materials for Photocatalytic H2 Evolution in the Presence of Sacrificial Electron Donors. *Angew. Chem., Int. Ed.* **2018**, *57*, 12106−12110.
(15) Côte, A. P.; Benin, A. I.; Ockwig, N. W.; O'Keeffe, M.; Matzger, A. J.; Yaghi, O. M. Porous, Crystalline, Covalent Organic Frameworks. *Science* **2005**, *310*, 1166−1170.
(16) Jin, E.; Asada, M.; Xu, Q.; Dalapati, S.; Addicoat, M. A.; Brady, M. A.; Xu, H.; Nakamura, T.; Heine, T.; Chen, Q.; Jiang, D. Two-dimensional sp(2) Carbon-Conjugated Covalent Organic Frameworks. *Science* **2017**, *357*, 673−676.
(17) Peng, Y.; Zhao, M.; Chen, B.; Zhang, Z.; Huang, Y.; Dai, F.; Lai, Z.; Cui, X.; Tan, C.; Zhang, H. Hybridization of MOFs and COFs: A New Strategy for Construction of MOF@COF Core-Shell Hybrid Materials. *Adv. Mater.* **2018**, *30*, No. 1770545.
(18) Sasmal, H. S.; Halder, A.; Kunjattu, H. S.; Dey, K.; Nadol, A.; Ajithkumar, T. G.; Ravindra Bedadur, P.; Banerjee, R. Covalent Self-Assembly in Two Dimensions: Connecting Covalent Organic Framework Nanospheres into Crystalline and Porous Thin Films. *J. Am. Chem. Soc.* **2019**, *141*, 20371−20379.
(19) Sun, Q.; Fu, C. W.; Aguila, B.; Perman, J.; Wang, S.; Huang, H. Y.; Xiao, F. S.; Ma, S. Pore Environment Control and Enhanced Performance of Enzymes Infiltrated in Covalent Organic Frameworks. *J. Am. Chem. Soc.* **2018**, *140*, 984−992.
(20) Li, H.; Pan, Q.; Ma, Y.; Guan, X.; Xue, M.; Fang, Q.; Yan, Y.; Valtchev, V.; Qiu, S. Three-Dimensional Covalent Organic Frameworks with Dual Linkages for Bifunctional Cascade Catalysis. *J. Am. Chem. Soc.* **2016**, *138*, 14783−14788.
(21) Yuan, C.; Wu, X.; Gao, R.; Han, X.; Liu, Y.; Long, Y.; Cui, Y. Nanochannels of Covalent Organic Frameworks for Chiral Selective Transmembrane Transport of Amino Acids. *J. Am. Chem. Soc.* **2019**, *141*, 20187−20197.
(22) Lin, G.; Ding, H.; Yuan, D.; Wang, B.; Wang, C. A Pyrene-Based Fluorescent Three-Dimensional Covalent Organic Framework. *J. Am. Chem. Soc.* **2016**, *138*, 3302−3305.
(23) Chen, Y.; Shi, Z. L.; Wei, L.; Zhou, B.; Tan, J.; Zhou, H. L.; Zhang, Y. B. Guest-Dependent Dynamics in a 3D Covalent Organic Framework. *J. Am. Chem. Soc.* **2019**, *141*, 3298−3303.
(24) Zeng, Y.; Zou, R.; Zhao, Y. Covalent Organic Frameworks for CO_2 Capture. *Adv. Mater.* **2016**, *28*, 2855−2873.
(25) Kang, Z.; Peng, Y.; Qian, Y.; Yuan, D.; Addicoat, M. A.; Heine, T.; Hu, Z.; Tee, L.; Guo, Z.; Zhao, D. Mixed Matrix Membranes (MMMs) Comprising Exfoliated 2D Covalent Organic Frameworks (COFs) for Efficient CO_2 Separation. *Chem. Mater.* **2016**, *28*, 1277−1285.
(26) Liu, M.; Jiang, K.; Ding, X.; Wang, S.; Zhang, C.; Liu, J.; Zhan, Z.; Cheng, G.; Li, B.; Chen, H.; Jin, S.; Tan, B. Controlling Monomer Feeding Rate to Achieve Highly Crystalline Covalent Triazine Frameworks. *Adv. Mater.* **2019**, *31*, No. 1807865.
(27) Yang, Y.; Faheem, M.; Wang, L.; Meng, Q.; Sha, H.; Yang, N.; Yuan, Y.; Zhu, G. Surface Pore Engineering of Covalent Organic Frameworks for Ammonia Capture through Synergistic Multivariate and Open Metal Site Approaches. *ACS Cent. Sci.* **2018**, *4*, 748−754.
(28) Mondal, S.; Mohanty, B.; Nurhuda, M.; Dalapati, S.; Jana, R.; Addicoat, M.; Datta, A.; Jena, B. K.; Bhaumik, A. A Thiadiazole-Based Covalent Organic Framework: A Metal-Free Electrocatalyst toward Oxygen Evolution Reaction. *ACS Catal.* **2020**, *10*, 5623−5630.
(29) Lohse, M. S.; Bein, T. Covalent Organic Frameworks: Structures, Synthesis, and Applications. *Adv. Funct. Mater.* **2018**, *28*, No. 1705553.
(30) Kim, D. H.; Han, Y. W.; Moon, D. K. A Comparative Investigation of Dibenzo[a,c]phenazine and Quinoxaline Donor−Acceptor Conjugated Polymers: Correlation of Planar Structure and Intramolecular Charge Transfer Properties. *Polymer* **2019**, *185*, No. 121906.
(31) Wan, S.; Gándara, F.; Asano, A.; Furukawa, H.; Saeki, A.; Dey, S. K.; Liao, L.; Ambrogio, M. W.; Botros, Y. Y.; Duan, X.; et al. Covalent Organic Frameworks with High Charge Carrier Mobility. *Chem. Mater.* **2011**, *23*, 4094−4097.

(32) Fu, J.; Yu, J.; Jiang, C.; Cheng, B. g-C_3N_4-Based Heterostructured Photocatalysts. *Adv. Energy Mater.* **2018**, *8*, No. 1701503.
(33) Shao, P.; Li, J.; Chen, F.; Ma, L.; Li, Q.; Zhang, M.; Zhou, J.; Yin, A.; Feng, X.; Wang, B. Flexible Films of Covalent Organic Frameworks with Ultralow Dielectric Constants under High Humidity. *Angew. Chem., Int. Ed.* **2018**, *57*, 16501−16505.
(34) Zhao, X.; Pachfule, P.; Li, S.; Langenhahn, T.; Ye, M.; Schlesiger, C.; Praetz, S.; Schmidt, J.; Thomas, A. Macro/Microporous Covalent Organic Frameworks for Efficient Electrocatalysis. *J. Am. Chem. Soc.* **2019**, *141*, 6623−6630.
(35) Liu, H.; Chu, J.; Yin, Z.; Cai, X.; Zhuang, L.; Deng, H. Covalent Organic Frameworks Linked by Amine Bonding for Concerted Electrochemical Reduction of CO_2. *Chem* **2018**, *4*, 1696−1709.
(36) Jakowetz, A. C.; Hinrichsen, T. F.; Ascherl, L.; Sick, T.; Calik, M.; Auras, F.; Medina, D. D.; Friend, R. H.; Rao, A.; Bein, T. Excited-State Dynamics in Fully Conjugated 2D Covalent Organic Frameworks. *J. Am. Chem. Soc.* **2019**, *141*, 11565−11571.
(37) Zeng, J.-Y.; Wang, X. S.; Xie, B. R.; Li, M. J.; Zhang, X. Z. Covalent Organic Framework for Improving Near-Infrared Light Induced Fluorescence Imaging through Two-Photon Induction. *Angew. Chem., Int. Ed.* **2019**, *58*, 2−10.
(38) Biswal, B. P.; Vignolo-Gonzalez, H. A.; Banerjee, T.; Grunenberg, L.; Savasci, G.; Gottschling, K.; Nuss, J.; Ochsenfeld, C.; Lotsch, B. V. Sustained Solar H2 Evolution from a Thiazolo[5,4-d]thiazole-Bridged Covalent Organic Framework and Nickel-Thiolate Cluster in Water. *J. Am. Chem. Soc.* **2019**, *141*, 11082−11092.
(39) Li, Q.; Lan, X.; An, G.; Ricardez-Sandoval, L.; Wang, Z.; Bai, G. Visible-Light-Responsive Anthraquinone Functionalized Covalent Organic Frameworks for Metal-Free Selective Oxidation of Sulfides: Effects of Morphology and Structure. *ACS Catal.* **2020**, *10*, 6664−6675.
(40) Stegbauer, L.; Schwinghammer, K.; Lotsch, B. V. A Hydrazone-based Covalent Organic Framework for Photocatalytic Hydrogen Production. *Chem. Sci.* **2014**, *5*, 2789−2793.
(41) Vyas, V. S.; Haase, F.; Stegbauer, L.; Savasci, G.; Podjaski, F.; Ochsenfeld, C.; Lotsch, B. V. A Tunable Azine Covalent Organic Framework Platform for Visible Light-Induced Hydrogen Generation. *Nat. Commun.* **2015**, *6*, No. 8508.
(42) Pachfule, P.; Acharjya, A.; Roeser, J.; Langenhahn, T.; Schwarze, M.; Schomacker, R.; Thomas, A.; Schmidt, J. Diacetylene Functionalized Covalent Organic Framework (COF) for Photocatalytic Hydrogen Generation. *J. Am. Chem. Soc.* **2018**, *140*, 1423−1427.
(43) Wang, X.; Chen, L.; Chong, S. Y.; Little, M. A.; Wu, Y.; Zhu, W. H.; Clowes, R.; Yan, Y.; Zwijnenburg, M. A.; Sprick, R. S.; Cooper, A. I. Sulfone-Containing Covalent Organic Frameworks for Photocatalytic Hydrogen Evolution From Water. *Nat. Chem.* **2018**, *10*, 1180−1189.
(44) Bi, S.; Yang, C.; Zhang, W.; Xu, J.; Liu, L.; Wu, D.; Wang, X.; Han, Y.; Liang, Q.; Zhang, F. Two-Dimensional Semiconducting Covalent Organic Frameworks via Condensation at Arylmethyl Carbon Atoms. *Nat. Commun.* **2019**, *10*, No. 2467.
(45) Jin, E.; Lan, Z.; Jiang, Q.; Geng, K.; Li, G.; Wang, X.; Jiang, D. 2D sp2 Carbon-Conjugated Covalent Organic Frameworks for Photocatalytic Hydrogen Production from Water. *Chem* **2019**, *5*, 1632−1647.
(46) Zhang, S.; Cheng, G.; Guo, L.; Wang, N.; Tan, B.; Jin, S. Strong-Base-Assisted Synthesis of a Crystalline Covalent Triazine Framework with High Hydrophilicity via Benzylamine Monomer for Photocatalytic Water Splitting. *Angew. Chem., Int. Ed.* **2020**, *59*, 6007−6014.
(47) Wang, Q.; Hisatomi, T.; Jia, Q.; Tokudome, H.; Zhong, M.; Wang, C.; Pan, Z.; Takata, T.; Nakabayashi, M.; Shibata, N.; Li, Y.; Sharp, I. D.; Kudo, A.; Yamada, T.; Domen, K. Scalable Water Splitting on Particulate Photocatalyst Sheets with A Solar-to-Hydrogen Energy Conversion Efficiency Exceeding 1. *Nat. Mater.* **2016**, *15*, 611−615.
(48) Chen, S.; Takata, T.; Domen, K. Particulate Photocatalysts for Overall Water Splitting. *Nat. Rev. Mater.* **2017**, *2*, No. 17050.
(49) Wang, H.; Qian, C.; Liu, J.; Zeng, Y.; Wang, D.; Zhou, W.; Gu, L.; Wu, H.; Liu, G.; Zhao, Y. Integrating Suitable Linkage of Covalent Organic Frameworks into Covalently Bridged Inorganic/Organic Hybrids toward Efficient Photocatalysis. *J. Am. Chem. Soc.* **2020**, *142*, 4862−4871.
(50) Feng, X.; Chen, L.; Honsho, Y.; Saengsawang, O.; Liu, L.; Wang, L.; Saeki, A.; Irle, S.; Seki, S.; Dong, Y.; Jiang, D. An Ambipolar Conducting Covalent Organic Framework with Self-Sorted and Periodic Electron Donor-Acceptor Ordering. *Adv. Mater.* **2012**, *24*, 3026−3031.
(51) Lu, M.; Liu, J.; Li, Q.; Zhang, M.; Liu, M.; Wang, J. L.; Yuan, D. Q.; Lan, Y. Q. Rational Design of Crystalline Covalent Organic Frameworks for Efficient CO_2 Photoreduction with H2O. *Angew. Chem., Int. Ed.* **2019**, *58*, 12392−12397.
(52) Pachfule, P.; Acharjya, A.; Roeser, J.; Sivasankaran, R. P.; Ye, M. Y.; Bruckner, A.; Schmidt, J.; Thomas, A. Donor-Acceptor Covalent Organic Frameworks for Visible Light Induced Free Radical Polymerization. *Chem. Sci.* **2019**, *10*, 8316−8322.
(53) Lei, K.; Wang, D.; Ye, L.; Kou, M.; Deng, Y.; Ma, Z.; Wang, L.; Kong, Y. A Metal-Free Donor-Acceptor Covalent Organic Framework Photocatalyst for Visible-Light-Driven Reduction of CO_2 with H_2O. *ChemSusChem* **2020**, *13*, 1725−1729.
(54) Li, H.; Shao, P.; Chen, S.; Li, G.; Feng, X.; Chen, X.; Zhang, H. J.; Lin, J.; Jiang, Y. B. Supramolecular Alternating Donor-Acceptor Assembly toward Intercalated Covalent Organic Frameworks. *J. Am. Chem. Soc.* **2020**, *142*, 3712−3717.
(55) Ghosh, S.; Nakada, A.; Springer, M. A.; Kawaguchi, T.; Suzuki, K.; Kaji, H.; Baburin, I.; Kuc, A.; Heine, T.; Suzuki, H.; Abe, R.; Seki, S. Identification of Prime Factors to Maximize the Photocatalytic Hydrogen Evolution of Covalent Organic Frameworks. *J. Am. Chem. Soc.* **2020**, *142*, 9752−9762.
(56) Li, S.; Li, L.; Li, Y.; Dai, L.; Liu, C.; Liu, Y.; Li, J.; Lv, J.; Li, P.; Wang, B. Fully Conjugated Donor−Acceptor Covalent Organic Frameworks for Photocatalytic Oxidative Amine Coupling and Thioamide Cyclization. *ACS Catal.* **2020**, *10*, 8717−8726.
(57) Golbeck, J. H.; Bryant, D. A. Photosystem I. *Curr. Top. Bioenerg.* **1991**, *16*, 83−177.
(58) Xu, Y.; Mao, N.; Zhang, C.; Wang, X.; Zeng, J.; Chen, Y.; Wang, F.; Jiang, J.-X. Rational Design of Donor-π-Acceptor Conjugated Microporous Polymers for Photocatalytic Hydrogen Production. *Appl. Catal., B* **2018**, *228*, 1−9.
(59) Auras, F.; Ascherl, L.; Hakimioun, A. H.; Margraf, J. T.; Hanusch, F. C.; Reuter, S.; Bessinger, D.; Doblinger, M.; Hettstedt, C.; Karaghiosoff, K.; Herbert, S.; Knochel, P.; Clark, T.; Bein, T. Synchronized Offset Stacking: A Concept for Growing Large-Domain and Highly Crystalline 2D Covalent Organic Frameworks. *J. Am. Chem. Soc.* **2016**, *138*, 16703−16710.
(60) Xu, Y. X.; Chueh, C. C.; Yip, H. L.; Ding, F. Z.; Li, Y. X.; Li, C. Z.; Li, X.; Chen, W. C.; Jen, A. K. Improved Charge Transport and Absorption Coefficient in Indacenodithieno[3,2-b]thiophene-based Ladder-type Polymer Leading to Highly Efficient Polymer Solar Cells. *Adv. Mater.* **2012**, *24*, 6356−6361.
(61) Wang, S.; Hai, X.; Ding, X.; Jin, S.; Xiang, Y.; Wang, P.; Jiang, B.; Ichihara, F.; Oshikiri, M.; Meng, X.; Li, Y.; Matsuda, W.; Ma, J.; Seki, S.; Wang, X.; Huang, H.; Wada, Y.; Chen, H.; Ye, J. Intermolecular Cascaded pi-Conjugation Channels for Electron Delivery Powering CO_2 Photoreduction. *Nat. Commun.* **2020**, *11*, No. 1149.
(62) Liao, J.; Xu, Y.; Zhao, H.; Zong, Q.; Fang, Y. Novel A-D-A Type Small Molecules with β-Alkynylated BODIPY Flanks for Bulk Heterojunction Solar Cells. *Org. Electron.* **2017**, *49*, 321−333.
(63) Zhou, P.; Zhang, Z.-G.; Li, Y.; Chen, X.; Qin, J. Thiophene-Fused Benzothiadiazole: A Strong Electron-Acceptor Unit to Build D−A Copolymer for Highly Efficient Polymer Solar Cells. *Chem. Mater.* **2014**, *26*, 3495−3501.
(64) Beaujuge, P. M.; Pisula, W.; Tsao, H. N.; Ellinger, S.; Mullen, K.; Reynolds, J. R. Tailoring Structure-Property Relationships in

https://dx.doi.org/10.1021/acscatal.0c04820
ACS Catal. 2021, 11, 2098−2107

Dithienosilole-Benzothiadiazole Donor-Acceptor Copolymers. *J. Am. Chem. Soc.* **2009**, *131*, 7514−7515.
(65) Jung, J. W.; Liu, F.; Russell, T. P.; Jo, W. H. Medium Bandgap Conjugated Polymer for High Performance Polymer Solar Cells Exceeding 9% Power Conversion Efficiency. *Adv. Mater.* **2015**, *27*, 7462−7468.
(66) Jung, J. W.; Liu, F.; Russell, T. P.; Jo, W. H. Anthracene-Based Medium Bandgap Conjugated Polymers for High Performance Polymer Solar Cells Exceeding 8% PCE Without Additive and Annealing Process. *Adv. Energy Mater.* **2015**, *5*, No. 1500065.
(67) Jordan, P.; Fromme, P.; Witt, H. T.; Klukas, O.; Saenger, W.; Krauss, N. Three-Dimensional Structure of Cyanobacterial Photosystem I at 2.5 A Resolution. *Nature* **2001**, *411*, 909−917.
(68) Kargul, J.; Janna Olmos, J. D.; Krupnik, T. Structure and Function of Photosystem I and Its Application in Biomimetic Solar-to-Fuel Systems. *J. Plant Physiol.* **2012**, *169*, 1639−1653.
(69) Matsumoto, Y. Energy Positions of Oxide Semiconductors and Photocatalysis with Iron Complex Oxides. *J. Solid State Chem.* **1996**, *126*, 227−234.
(70) Shi, L.; Wang, T.; Zhang, H.; Chang, K.; Ye, J. Electrostatic Self-Assembly of Nanosized Carbon Nitride Nanosheet onto a Zirconium Metal-Organic Framework for Enhanced Photocatalytic CO_2 Reduction. *Adv. Funct. Mater.* **2015**, *25*, 5360−5367.
(71) Wang, X.; Blechert, S.; Antonietti, M. Polymeric Graphitic Carbon Nitride for Heterogeneous Photocatalysis. *ACS Catal.* **2012**, *2*, 1596−1606.
(72) Shang, J.; Ma, L.; Li, J.; Ai, W.; Yu, T.; Gurzadyan, G. G. The Origin of Fluorescence from Graphene Oxide. *Sci. Rep.* **2012**, *2*, No. 792.
(73) Wang, X.; Maeda, K.; Thomas, A.; Takanabe, K.; Xin, G.; Carlsson, J. M.; Domen, K.; Antonietti, M. A Metal-free Polymeric Photocatalyst for Hydrogen Production from Water under Visible Light. *Nat. Mater.* **2009**, *8*, 76−80.
(74) Calle-Vallejo, F.; Tymoczko, J.; Colic, V.; Vu, Q. H.; Pohl, M. D.; Morgenstern, K.; Loffreda, D.; Sautet, P.; Schuhmann, W.; Bandarenka, A. S. Finding Optimal Surface Sites on Heterogeneous Catalysts by Counting Nearest Neighbors. *Science* **2015**, *350*, 185−189.
(75) Wan, Y.; Wang, L.; Xu, H.; Wu, X.; Yang, J. A Simple Molecular Design Strategy for Two-Dimensional Covalent Organic Framework Capable of Visible-Light-Driven Water Splitting. *J. Am. Chem. Soc.* **2020**, *142*, 4508−4516.
(76) Deibel, C.; Strobel, T.; Dyakonov, V. Role of the Charge Transfer State in Organic Donor-Acceptor Solar Cells. *Adv. Mater.* **2010**, *22*, 4097−4111.
(77) Lan, Z. A.; Zhang, G.; Chen, X.; Zhang, Y.; Zhang, K. A. I.; Wang, X. Reducing the Exciton Binding Energy of Donor-Acceptor-Based Conjugated Polymers to Promote Charge-Induced Reactions. *Angew. Chem., Int. Ed.* **2019**, *58*, 10236−10240.
(78) Lan, Z.-A.; Ren, W.; Chen, X.; Zhang, Y.; Wang, X. Conjugated Donor-Acceptor Polymer Photocatalysts with Electron-Output "Tentacles" for Efficient Hydrogen Evolution. *Appl. Catal., B* **2019**, *245*, 596−603.

https://dx.doi.org/10.1021/acscatal.0c04820
ACS Catal. 2021, 11, 2098−2107